Research Article

Optimization Control Strategy for Islanded Parallel Virtual Synchronous Generators

Hailin Hu [iD],[1,2] **Fu Feng** [iD],[1] **Tao Wang** [iD],[1] **Xiaofeng Wan** [iD],[3] **and Xiaohua Ding** [iD][3]

[1]*School of Electrical Engineering and Automation, Jiangxi University of Science and Technology, Ganzhou 341000, Jiangxi, China*
[2]*Maglev Engineering Research Center, National University of Defense Technology, Changsha 410005, Hunan, China*
[3]*School of Information Engineering, Nanchang University, Nanchang 330031, Jiangxi, China*

Correspondence should be addressed to Hailin Hu; jackyhhl@163.com

Virtual Synchronous Generators (VSGs) can reduce the frequency and power oscillation in the grid. For parallel multi-VSGs in island microgrid, the differences of equivalent output impedance and line impedance affect the orderly sharing of reactive power and restraining of circulating current greatly. The power sharing and circulating current characteristics of VSGs are analyzed in this paper. To solve this problem, an optimization control method for parallel VSGs is proposed, which included the inner voltage and current loop and the outer reactive power loop. In the inner voltage and current loop, a virtual complex impedance including a resistive component and an inductive component is introduced. It reduces the coupling between active power and reactive power, and it reduces the disorderly distribution of power due to impedance differences. In the reactive power loop, the output voltage feedback and integrator links are adopted, which reduce the deviation of output voltage and restrain circulating current. The effects on the equivalent output impedance in the different control parameters and virtual complex impedance are analyzed, the effects on system stability in the different resistive components of virtual complex impedance are analyzed, and the proper parameters are selected. Simulation and experimental results show the correctness and validity of the proposed control method.

1. Introduction

By increasing the inertia and damping links in an active power control loop, the grid support capability in a weak grid of virtual synchronous generators (VSGs) is summarized in [1, 2]. When multiple VSGs are operated in parallel, there are differences in the output voltage, equivalent output impedance, and connection line impedance of the individual VSGs, which are caused by the different controller parameters, nonlinearities in the power devices, differences in filter parameters, and the distance from the grid connection point. These differences affect the accuracy of power distribution, increase the fundamental current circulation between the VSGs, and may cause overcurrent faults [3]. Therefore, it is of great value to study the power distribution and current circulation suppression between parallel VSGs. [4, 5].

Focusing on the power distribution problem of parallel VSGs, in [6], an integral controller is added in the reactive power loop to eliminate the influence of connection line impedance on reactive power distribution. However, the coupling of active and reactive power is not considered. In [7], a feedforward angular frequency is added to the power frequency link to realize switching under different operation modes. A small-signal model and several constraints are used to optimize the dynamic and static characteristics of the parameters, but the implementation method is complicated. In [8], function terms for the power and droop coefficient in traditional droop control are introduced. This improved the dynamic regulation performance, but it did not eliminate the steady-state error caused by the connection line impedance. In [9], a new multiloop control strategy is described, the virtual reactance can be selected according to the external inductance, but the conturation principle of virtual

impedance in parallel VSGs is not considered. In [10], a joint control method for the virtual inductor and external output inductor is proposed, which is used to improve the applicability of the inverter P-f and Q-V droop control in medium- and low-voltage networks. However, it is difficult to obtain the external output inductance accurately, and the method is not practical. In [11], a parallel VSGs control method based on virtual impedance is proposed. This approach improves the excitation link to achieve adequate control of the AC bus voltage, but the power coupling problem is not considered. In [12], a consistency-based parallel VSGs distributed control method is described. Although this enhances the system frequency and active power characteristics, it requires communication between the parallel VSGs.

This paper describes a method that improves the traditional virtual synchronous power generation technology, based on analysis of the parallel operation characteristics of multiple VSGs. The optimization control strategy includes the outer reactive power loop and the inner voltage and current loop. In the inner voltage and current loop, a virtual complex impedance including a resistive component and an inductive component is introduced. It reduces the effects on decoupling between active power and reactive power, and it reduces the effects on accurate power sharing due to the impedance difference. In the reactive power loop, the output voltage feedback and integrator links are adopted, which will reduce the deviation of output voltage and restrain circulating current.

2. Operating Characteristics of Parallel VSGs

Figure 1 shows the simplified structure of a traditional parallel VSGs system. For a single VSG, it connects to the AC bus through the connection line and grid-connected switch. Z_{line} is the impedance of the connection line, and K is the grid-connected switch. Z_{load} is the common load, L_1 is the filter inductance, and R_1 is the sum of the equivalent internal resistance of the filter inductance and the equivalent internal resistance of the power device. U_C is the VSG output capacitor voltage, also known as the terminal voltage. I_2 is the grid-side output current, and I_1 is the converter-side current.

A simple model with two parallel VSGs is shown in Figure 2. U_1 and U_2 are the voltage amplitudes of the VSG bridge arms' midpoint, E is the AC bus voltage amplitude, Z_o is the equivalent output impedance of the VSG ($Z_o = R_o + jX_o$), and Z_{line} is the connection line impedance ($Z_{\text{line}} = R_{\text{line}} + jX_{\text{line}}$).

The transmission impedance Z is equal to the sum of the equivalent output impedance and the connection line impedance, φ is the transmission impedance phase angle, and θ is the phase angle difference between the bus voltage and the voltage of the bridge arm's midpoint. I_o and I_L represent the output current of the VSG and load current.

2.1. Analysis of VSG Power Transmission Characteristics.

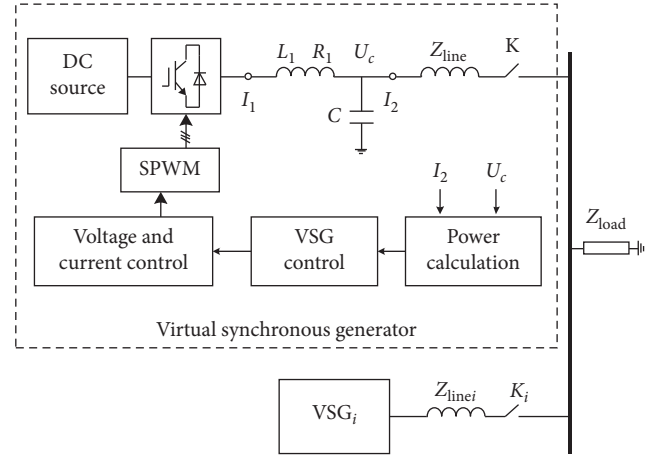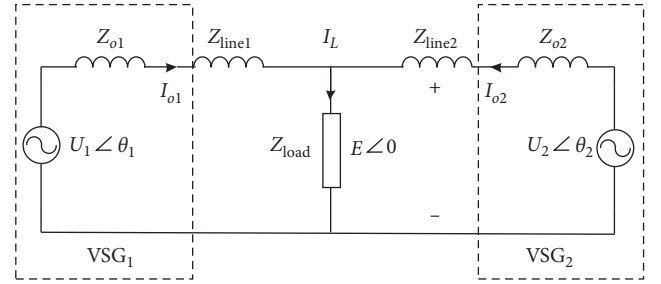

Figure 1: Structure diagram of parallel VSGs.

Figure 2: Two VSG parallel models.

The output active power and reactive power of VSG i ($i = 1, 2$) can be expressed as follows:

$$P_i = \left(\frac{U_i E}{Z_i} \cos \theta_i - \frac{E^2}{Z_i} \right) \cos \varphi_i + \frac{U_i E}{Z_i} \sin \theta_i \sin \varphi_i,$$

$$Q_i = \left(\frac{U_i E}{Z_i} \cos \theta_i - \frac{E^2}{Z_i} \right) sin\varphi_i - \frac{U_i E}{Z_i} \sin \theta_i \sin \varphi_i. \tag{1}$$

According to (1), the output active power and reactive power are related to the voltage amplitude and phase angle difference and are affected by the transmission impedance. By setting the voltage and current control loop parameters, the equivalent output impedance of the VSG can be controlled, so that the equivalent output inductive reactance is much larger than the equivalent output resistive impedance, $X_o \gg R_o$. The transmission impedance of different voltage levels has different impedance ratios. In low-voltage distribution networks, the resistive impedance is much larger than the inductive impedance, $X_{\text{line}} \ll R_{\text{line}}$. In medium-voltage distribution networks, $X_{\text{line}} \approx R_{\text{line}}$. This causes the transmission impedance to exhibit complex characteristics. To decouple the active power from the reactive power, the transmission impedance is set to be inductive using virtual impedance technology. The power transmission is approximately shown as follows:

$$P_i = \frac{U_i E}{X_{oi} + X_{\text{line}i}} \theta_i,$$

$$Q_i = \frac{E(U_i - E)}{X_{oi} + X_{\text{line}i}}. \tag{2}$$

From the abovementioned analysis, when the transmission impedance is inductive, the active power transmission is mainly affected by the voltage phase angle, whereas the reactive power transmission is affected by the voltage amplitude. [13] The active power and reactive power are approximately decoupled.

The VSG power control equation can be described as follows:

$$J \frac{d\omega}{dt} = \frac{P^*}{\omega_n} - \frac{P_i}{\omega_n} + D_p (\omega_n - \omega_i),$$

$$U_i = E_n + D_q (Q^* - Q_i), \tag{3}$$

where J is the virtual inertia, P^* is the reference value of active power, P_i is the actual output active power, D_P is the damping coefficient, ω_n is the rated angular frequency, and ω_i is the virtual angular frequency. U_i is the amplitude of VSG output voltage, E_n is the rated voltage amplitude, D_q is the reactive power droop coefficient, Q^* is the reference value of reactive power, and Q_i is the actual output reactive power. Combining equations (2) and (3), the VSG active power closed-loop control diagram is shown as Figure 3. The reactive power closed-loop control diagram is shown as Figure 4.

There is an integral link in the active loop of the virtual synchronous control strategy; when the VSG runs in the steady state, the input of the integral link is 0.

$$P_i = P^* + D_p (\omega_n - \omega_i). \tag{4}$$

According to (4), when the transmission impedance of the VSG is inductive, the active power distribution is related to the active power command value and the active-frequency droop coefficient, and active power distribution is not affected by transmission impedance.

For two VSGs with the same rated capacity, as long as the active power command value and the active-frequency droop coefficient are equal, the active power can be divided equally. Therefore, the active power transmission is highly robust.

Similarly, the VSG output reactive power equation can be obtained as follows:

$$Q_i = \frac{\left(E_n - E + Q^* D_q\right)\left(E/X_i\right)}{\left(1 + (E/X_i) D_q\right)}. \tag{5}$$

According to (5), the reactive power distribution is affected by the droop coefficient, the reactive power reference value, and the transmission impedance. When the reactive power of two VSGs with equal capacity is evenly distributed, the droop coefficients, reactive power setting values, and
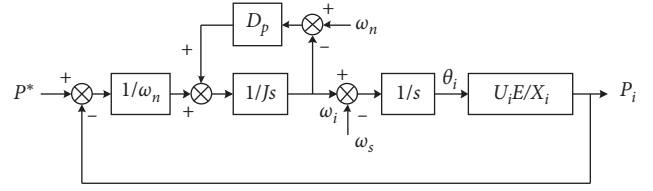

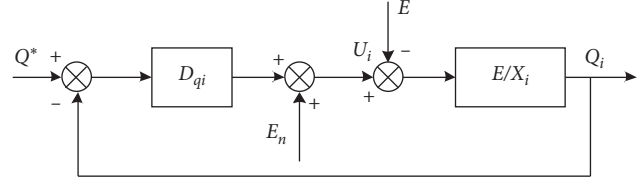FIGURE 3: Active power closed-loop control diagram of the VSG.

FIGURE 4: Reactive power closed-loop control diagram of the VSG.

transmission impedances of each VSG must be equal. When the actual system is running, the system interference, the nonlinearity of the power device, the parameter offset, and the difference in connection impedance make it difficult to meet the conditions for the orderly distribution of reactive power.

2.2. Analysis of Current Circulation Characteristics of the VSG.
The output current characteristics of parallel VSGs are analyzed in the fundamental wave frequency domain. Equation (6) can be obtained from Figure 2.

$$\begin{cases} U_1 \angle \theta_1 - Z_{\text{line}1} I_{o1} = E \angle 0, \\\\ U_2 \angle \theta_2 - Z_{\text{line}2} I_{o2} = E \angle 0, \\\\ I_{o1} + I_{o2} = I_L = E \angle \dfrac{0}{Z_{\text{load}}}. \end{cases} \tag{6}$$

In the abovementioned equations, the transmission impedance is the sum of the equivalent output impedance and the connection line impedance, $Z_i = Z_{oi} + Z_{\text{line}i}$. If the equivalent output impedance and connection line impedance of the two VSGs are equal, the following equation can be obtained:

$$\begin{cases} I_{o1} = \dfrac{U_1 \angle \theta_1 - U_2 \angle \theta_2}{2 Z_1} + \dfrac{E}{2 Z_{\text{load}}}, \\\\ I_{o2} = \dfrac{U_2 \angle \theta_2 - U_1 \angle \theta_1}{2 Z_1} + \dfrac{E}{2 Z_{\text{load}}}. \end{cases} \tag{7}$$

When the equivalent output impedance of the VSG is inductive and the connection line impedance is far less than the equivalent output impedance, the transmission impedance is approximately equal to the equivalent output impedance, $Z_i \approx X_{oi}$, and the following equation can be obtained:

$$\begin{cases} I_{o1} = \dfrac{U_1 \angle \theta_1 - U_2 \angle \theta_2}{2jX_{o1}} + \dfrac{E}{2Z_{\text{load}}} = I_{H1} + I_{oL1}, \\[3mm] I_{o2} = \dfrac{U_2 \angle \theta_2 - U_1 \angle \theta_2}{2jX_{o1}} + \dfrac{E}{2Z_{\text{load}}} = I_{H2} + I_{oL2}. \end{cases} \tag{8}$$

According to equation (8), as the equivalent output impedance of the two VSGs is inductive and equal and the connection line impedance is much smaller than the equivalent output impedance, the output current of the VSG includes two components: the load current I_{oL} and the circulation current I_H. The load current is distributed equally, and the circulating current is determined by the output voltage amplitude difference, phase difference, and equivalent output impedance of the parallel VSGs. [13].

The fundamental circulating current between two VSGs is defined as follows:

$$I_H = \frac{I_{o1} - I_{o2}}{2} = \frac{U_1 \angle \theta_1 - U_2 \angle \theta_2}{2jX_{o1}}. \tag{9}$$

If the virtual voltage amplitude of the VSGs is equal, there is only a phase difference, and the phase difference will cause active power circulation, which will transfer active current circulation from the advanced phase part to the delayed phase part in the parallel VSGs. If the virtual voltage phase of the VSG is equal, there is only an amplitude difference, and the reactive current circulation will flow from the high-voltage amplitude part to the low-voltage amplitude part. The output impedance of the VSG with high-voltage amplitude is inductive, and the output impedance of the VSG with low-voltage amplitude is capacitive. If both the amplitude and phase of the output voltages of the two VSGs are not equal, then the circulating current contains both active and reactive components [14].

From the analysis of the current circulation characteristics, it can be seen that the current circulation of the parallel VSGs is suppressed by achieving the output voltage and transmission impedance of the two VSGs is equal. The suppression of the current circulation can also be realized by increasing the equivalent output impedance.

3. Optimization Control Strategy of Parallel VSGs

3.1. Introduction of Virtual Impedance. From the analysis in the previous section, the active power and the reactive power

are decoupled by setting the transmission impedance to be purely resistive or purely inductive, and this is the premise of independent control of active power and reactive power. Increasing the equivalent output impedance of the virtual synchronous generator can reduce the current circulation caused by the difference between the equivalent output impedance and the connection impedance. To change the transmission impedance characteristics of the VSG, the output current of the grid side is used as the feedback, and a virtual complex impedance consisting of resistance and inductive components is introduced. The negative resistive virtual impedance is used to reduce the resistive component of transmission impedance, and the transmission impedance is approximately purely inductive. It can reduce the coupling of active power and reactive power transmission. The positive inductive virtual impedance is introduced, the transmission impedance increases, and the current circulation caused by differences in the equivalent output impedance and connection line impedance is reduced. After introducing the virtual complex impedance, the voltage compensation is shown as follows:

$$\begin{cases} u_{vd} = R_{vd} i_{2d} - \omega L_{vd} i_{2q}, \\[2mm] u_{vq} = R_{vq} i_{2q} + \omega L_{vq} i_{2d}, \end{cases} \tag{10}$$

where R_{vq} and R_{vd} are the virtual impedances in the dq rotation coordinates. To reduce the resistive component of the equivalent output impedance, the virtual impedance R_v takes a negative value, and L_{vq} and L_{vd} are the virtual inductive resistances in the dq coordinates [13].

To increase the control precision and control the current circulation, the voltage-type VSG structure is adopted, and the terminal voltage control loop is added after the power control loop. The structure of the inner voltage and current control loop with virtual complex impedance is shown as Figure 5.

In Figure 5, k_{uP} and K_{ui} are the proportional (P) and integral (I) gains of the voltage-loop PI controller, k_{iP} is the proportional gain of the current inner loop, k_{Pwm} is the converter gain, $Z_v(s)$ is the virtual complex impedance ($Z_v(s) = R_v + L_v s$), u^* is the voltage-loop voltage command value, u_v^* is the voltage-loop reference value after introducing the virtual impedance, u is the output voltage, i_1 is the converter-side current, and i_2 is the grid-side output current. A mathematical model of the output voltage can be established according to Figure 5. When the virtual impedance is not introduced, it can be written as follows:

$$CsU(s) = \left\{ \left[\left(U^*(s) - U(s) \right) \left(\frac{k_{up} + k_{ui}}{s} \right) - \left(I_2(s) + U(s)Cs \right) \right] k_{ip} k_{pwm} - U(s) - \frac{(L_1 s + R_1) I_2(s)\}}{L_1 s + R_1} \right\}. \tag{11}$$
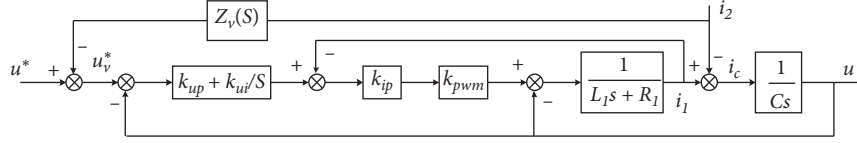
FIGURE 5: Voltage and current loop structure after adding virtual impedance.

Equation (11) can be transformed into the following equation:

$$U(s) = \frac{\left[k_{ip}k_{pwm}\left(k_{up}s + k_{ui}\right)\right]U^*(s)}{L_1Cs^3 + \left(k_{ip}k_{pwm} + R_1\right)Cs^2 + \left(k_{ip}k_{pwm}k_{up} + 1\right)s + k_{ip}k_{pwm}k_{ui}},$$

$$- \frac{\left[L_1s^2 + \left(k_{ip}k_{pwm} + R_1\right)s\right]I_2(s)}{L_1Cs^3 + \left(k_{ip}k_{pwm} + R_1\right)Cs^2 + \left(k_{ip}k_{pwm}k_{up} + 1\right)s + k_{ip}k_{pwm}k_{ui}}. \tag{12}$$

It is equivalent to the following equation:

$$U(s) = G(s)U^*(s) - Z_o(s)I_2, \tag{13}$$

where $G(x)$ is the equivalent closed-loop voltage gain and $Z_0(s)$ is the equivalent output impedance. These terms can be written as follows:

$$G(s) = \frac{\left[k_{ip}k_{pwm}\left(k_{up}s + k_{ui}\right)\right]}{\left[L_1Cs^3\left(k_{ip}k_{pwm} + R_1\right)Cs^2 + \left(k_{ip}k_{pwm}k_{up} + 1\right)s + k_{ip}k_{pwm}k_{ui}\right]},$$

$$Z_o(s) = \frac{\left[L_1s^2 + \left(k_{ip}k_{pwm} + R_1\right)s\right]}{\left[L_1Cs^3 + \left(k_{ip}k_{pwm} + R_1\right)Cs^2 + \left(k_{ip}k_{pwm}k_{up} + 1\right)s + k_{ip}k_{pwm}k_{ui}\right]}. \tag{14}$$

After adding the virtual impedance, the following equation can be obtained:

$$U_v^*(s) = U^*(s) - Z_v(s)I_2(s). \tag{15}$$

Substituting (16) into (13) gives

$$U(s) = G(s)\left[U^* - Z_v(s)I_2\right] - Z_o(s)I_2,$$
$$= G(s)U^* - \left[G(s)Z_v(s) + Z_o(s)\right]I_2, \tag{16}$$

where $G(s)Z_v(s) + Z_0(s)$ is the equivalent output impedance after adding the virtual complex impedance and $Z_0'(s)$ is shown as the following equation:

$$Z_0'(s) = G(s)Z_v(s) + Z_o(s). \tag{17}$$

According to equation (15) and the parameters in Table 1, the equivalent output impedance can be illustrated using a Bode diagram without the added virtual impedance. Figure 6 is the equivalent output impedance Bode diagram for $K_{ui} = 0, 100, 500,$ and 1000. It can be seen that when $K_{ui} = 0$, the low-frequency equivalent output impedance is resistive, and it is the complex impedance characteristic at the fundamental frequency. When $K_{ui} = 500$, the equivalent output impedance is inductive at the fundamental frequency. The larger the value of K_{ui}, the wider the frequency band that belongs to the inductive output impedance. After the introduction of the virtual inductive impedance L_v, the equivalent output impedance is inductive at low and fundamental frequencies. The fundamental output impedance is approximately equal to the virtual inductive impedance L_v, which weakens the effect of changes in the filter inductance parameters on the output impedance. Therefore, the equivalent output impedance at the fundamental frequency can be designed by introducing a virtual complex impedance to match the impedance of the parallel VSGs, and the aim of improving power distribution accuracy and current circulation suppression can be achieved.

When selecting the virtual negative impedance R_v, the power decoupling and system stability requirements must be comprehensively considered. After introduction of the virtual impedance, the equivalent output impedance of the VSG at the fundamental frequency is approximately equal to the virtual impedance, so the transmission impedance at the fundamental frequency is given as follows:

$$Z(s) = Z_v(s) + Z_{\text{line}}(s) = \left(R_{\text{line}} + R_v\right) + s\left(L_{\text{line}} + L_v\right). \tag{18}$$

The formula $R_v = -R_{\text{line}}$ is established, and active power and reactive power transmission can achieve decoupling.

Parameter/unit	Value
L_1/mh	5
R_1/Ω	0.1
C/uf	10
Z_{line}/Ω	$0.5 + 0.06j$
L_v/mh	1
k_{up}	0.3
k_{ui}	600
k_{ip}	2
k_{pwm}	250
R_v/Ω	-0.4

FIGURE 6: Equivalent output impedance Bode diagram with no virtual impedance.

The resistive component of transmission impedance has a damping effect on nonfundamental frequency disturbances. In the resistive component of transmission impedance setting, both the power decoupling and the nonfundamental frequency stability should be taken into consideration. The equivalent output impedance of the VSG after introducing the virtual impedance can be expressed as follows:

$$Z(s) = Z_o'(s) + Z_{\text{line}}(s),$$
$$= G(s)Z_v(s) + Z_o(s) + Z_{\text{line}}(s). \tag{19}$$

The relationship between the output harmonic current $i_d(s)$ and the voltage disturbance $u_d(s)$ is shown as follows:

$$\frac{i_d(s)}{u_d(s)} = \frac{1}{Z(s)} = Y(s). \tag{20}$$

Therefore, the stability of the system can be analyzed by identifying the distribution of the characteristic roots of the characteristic equation. Combining (17), (18), and (20), the following equation can be obtained:

$$Y(s) = \frac{T(s)}{\left[(L_{\text{line}}s + R_{\text{line}})T(s) + k_{ip}k_{pwm}(k_{up}s + k_{ui})(L_v s + R_v) + L_1 s^2 + (k_{ip}k_{pwm} + R_1)s\right]}, \tag{21}$$

$$T(s) = L_1 C s^3 + (k_{ip}k_{pwm} + R_1)C s^2 + (k_{ip}k_{pwm}k_{up} + 1)s + k_{ip}k_{pwm}k_{ui}.$$

When $R_{\text{line}} = 0.5\,\Omega$ and $L_{\text{line}} = 0.4$ mh, according to the parameters in Table 1, the root locus of $Y(s)$ with respect to R_v is shown in Figure 7. The pole S_1 determines the stability of $Y(S)$. As R_v increases, S_1 moves to the right of the complex plane and reaches the origin when $R_v = -0.5\,\Omega$. Therefore, $|R_v|$ should not be too large, it should be kept at a certain difference with R_{line}, so as S_1 has a certain distance from the imaginary axis, and the system has a certain stability margin.

3.2. Reactive Power Loop Improvement. From the analysis in the previous section, it is known that the transmission of active power and reactive power is decoupled, when the transmission impedance of the VSG is inductive. Due to the integration link 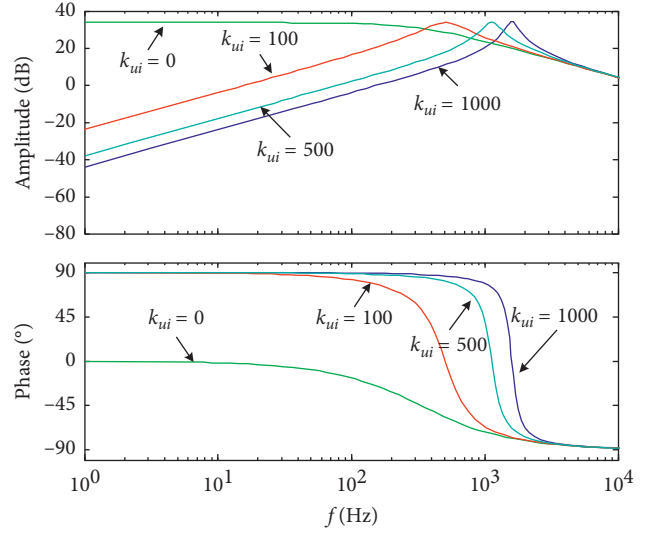in the active power loop, the active power allocation of the parallel VSGs is related to the active power reference value and the active power droop coefficient, and it is not affected by the transmission impedance. The reactive power distribution is affected not only by the droop coefficient but also by the reactive power reference value and the transmission impedance. At the same time, the load voltage fluctuates because of the load fluctuation and the droop characteristics of the reactive power loop. The fluctuations of load voltage can be restrained, and the output voltage can be stabilized within a certain range by introducing a negative feedback link $K_e(E^* - E)$ in the reactive power loop (here, K_e is the feedback coefficient, E^* is the reference value of the load voltage, and E is the actual value of the load voltage). The integral link is introduced into the power loop, and it achieves the decoupling of reactive power and transmission impedance.
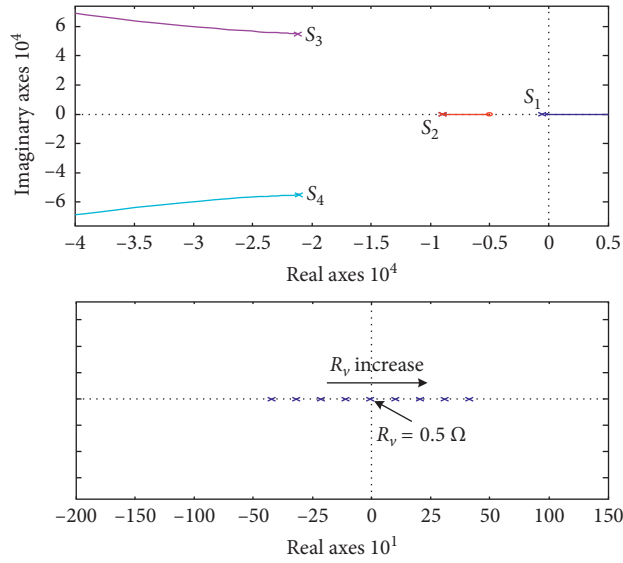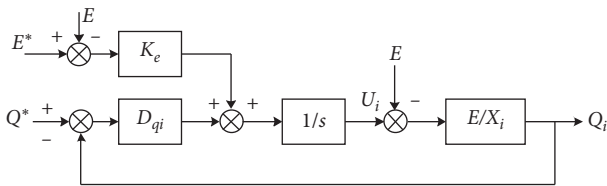
Figure 7: Root locus of $Y(s)$ for increasing R_v.

Figure 8: Improved virtual synchronous reactive power-voltage control block diagram.

Figure 9: Structure of the inner voltage and current loop.

The improved reactive power control loop structure is shown in Figure 8. When the system is stable, the input of the integration link is 0. The expression of power and voltage is shown as follows:

$$D_{qi}\left(Q_i - Q^*\right) = K_e\left(E^* - E\right). \tag{22}$$

From equation (22), it can be determined that the reactive power distribution is related to the droop coefficient, reactive power reference value, and voltage feedback coefficient.

It is independent of the transmission impedance. As long as the voltage feedback coefficients are equal and the reactive power reference value and droop coefficient are set in inverse proportion to the rated capacity, the ordered distribution of reactive power can be achieved [15, 16].

3.3. Structure of Optimization Control Strategy. A structure diagram of the inner voltage and current control loop is shown in Figure 9. The terminal voltage is controlled in the synchronous rotating coordinate system.

The terminal voltage loop adopts the PI regulator, the current loop adopts the P regulator, and the decoupling compensation is added to the controller to eliminate the cross coupling of the dq-axis voltage and current, and it
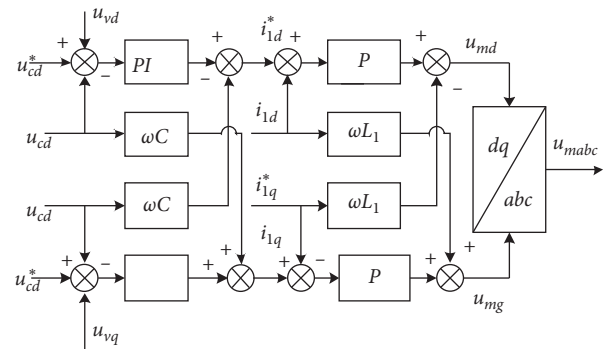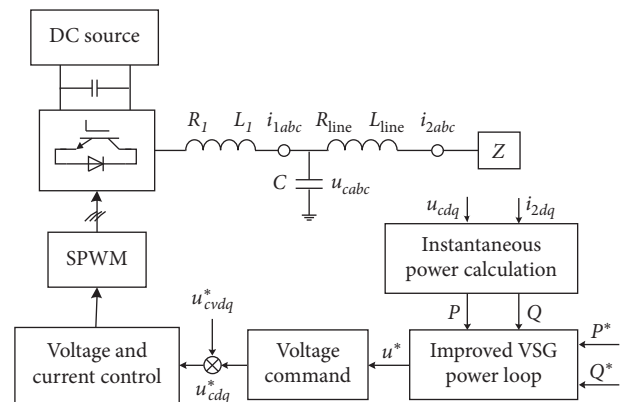

Figure 10: Improved parallel virtual synchronization control strategy.

improves the system dynamic performance. In the figure, the subscripts "d" and "q" indicate the synchronous rotation dq coordinates, U_{cdq} and i_{ldq} are the terminal voltage and

converter-side current in the synchronous rotation dq co-ordinate system, and ω is the virtual electrical angular frequency of the VSG [17, 18].

The improved control strategy of parallel VSGs is illustrated in Figure 10. In the figure, L_1 is the output filter inductor, R_1 is the sum of the internal resistance of the filter inductor and the internal resistance of the power device, C is the filter capacitor, and L_{line} and R_{line} are the connection line impedances. i_{1abc} is the inductor current on the converter side, i_{2abc} is the load current, and u_{cabc} is the voltage of capacitor.

The instantaneous power P and Q calculation formulas are shown as equation (23), and the reference value U^* of the midpoint voltage of the bridge arm is obtained by the improved power loop.

$$\begin{cases} P = 1.5\left(u_{cd}i_{2d} + u_{cq}i_{2q}\right), \\ Q = 1.5\left(u_{cd}i_{2d} - u_{cd}i_{2q}\right), \end{cases} \tag{23}$$

where U_{cd} and U_{cq} are the d and q coordinate components of the filter capacitor voltage U_c, while i_{2d} and i_{2q} are the d and q coordinate components of the load current i_2.

Ignoring the role of the filter capacitor C, the relationship among the bridge midpoint voltage, terminal voltage, and output current of the converter side is given by equation (24). The relationships between voltage and current in the dq coordinate system are given by equations (25) and (26) [11].

$$u_{cabc} = u_{abc} - R_1 i_{1abc} - L_1 \frac{\mathrm{d}i_{1abc}}{\mathrm{d}t}, \tag{24}$$

$$\begin{bmatrix} u_{cd} \\ u_{cq} \end{bmatrix} = \begin{bmatrix} u_d \\ u_q \end{bmatrix} - Y^{-1} \begin{bmatrix} i_{1d} \\ i_{1q} \end{bmatrix}, \tag{25}$$

$$\begin{cases} Y = \frac{1}{R_1^2 + X_1^2} \begin{bmatrix} R_1 & X_1 \\ -X_1 & R_1 \end{bmatrix}, \\ \begin{bmatrix} u_d \\ u_q \end{bmatrix} = \begin{bmatrix} E\cos\varphi \\ E\sin\varphi \end{bmatrix}, \end{cases} \tag{26}$$

where i_{1d} and i_{1q} are the output currents of the converter side in the dq coordinate system, U_d and U_q are the dq-axis components obtained by dq decomposition of the midpoint voltage of the bridge arm using the terminal voltage vector orientation, U_{cd} and U_{cq} are the dq-axis components of the terminal voltage, Y is the filter impedance matrix, and X_1 is the inductive reactance ($X_1 = \omega L_1$). The phase angle φ represents the phase angle difference between the bridge midpoint voltage vector and the terminal voltage vector, which is equal to the integral of the difference between the virtual rotor angular velocity ω and the terminal voltage electrical angular velocity ω_c of the virtual synchronous control [18].

The reference value of the terminal voltage under the synchronous rotation coordinates is shown as equation (25). The terminal voltage is sent to inner the voltage current

TABLE 2: System simulation parameters.

Parameter/unit	Value
U_{dc}/V	600
U/V	380
J, D_p	0.05, 15
D_q	480
P^*/kW	9
Q^*/kvar	6
L_v/mh	1
P_0/kW	4
$Q_0 Q_0$/kvar	3
L_1/mh, R_1/Ω	5, 0.1
L_2/mh, R_2/Ω	4.8, 0.1
Z_{line1}/Ω	$0.45 + 0.06j$
Z_{line2}/Ω	$0.55 + 0.07j$
R_v/Ω	-0.2

control loop to get the modulation voltage, the control signals of power components are obtained through sinusoidal pulse width modulation, and power equipartitioning and circulating current suppression of the parallel VSGs are realized.

4. Simulation and Experiment

The model of two parallel VSGs is constructed in the Matlab/Simulink environment to verify the effectiveness of improved control strategy. The main parameters are listed in Table 2. The total simulation time of the system is 2 seconds. From the start to 0.6 s, the first VSG runs alone, the other VSG is connected at 0.6 s, and the first VSG exits at 1.2 s.

Figure 11 shows the simulation results of the voltage, current, and circulating current when two parallel VSGs are running with the traditional control strategy and the improved control strategy.

Figure 12 shows the output power results of two VSGs with optimization control strategy.

Due to the influence of impedance differences, the circulating current of parallel VSGs with traditional control strategy is relatively large, and the reactive power equipartitioning cannot be achieved.

The dynamic current dividing response time of the improved control strategy is shorter, the amplitude of the circulating current is smaller in the steady state, and the effect of reactive power distribution is significantly improved.

The experimental platform of two parallel VSGs is shown in Figure 13, and the main parameters of the experiment are presented in Table 3. In the parallel VSGs experiment, the public load is 3 kW. During the experiment, an inverter works alone at the beginning, and another VSG is connected after a while.

Figure 14 shows the output current and circulating current waveforms of two parallel VSGs with the traditional control strategy and the improved control strategy. Compared with the traditional control strategy, the improved control strategy can respond more quickly, and the circulating current is smaller.
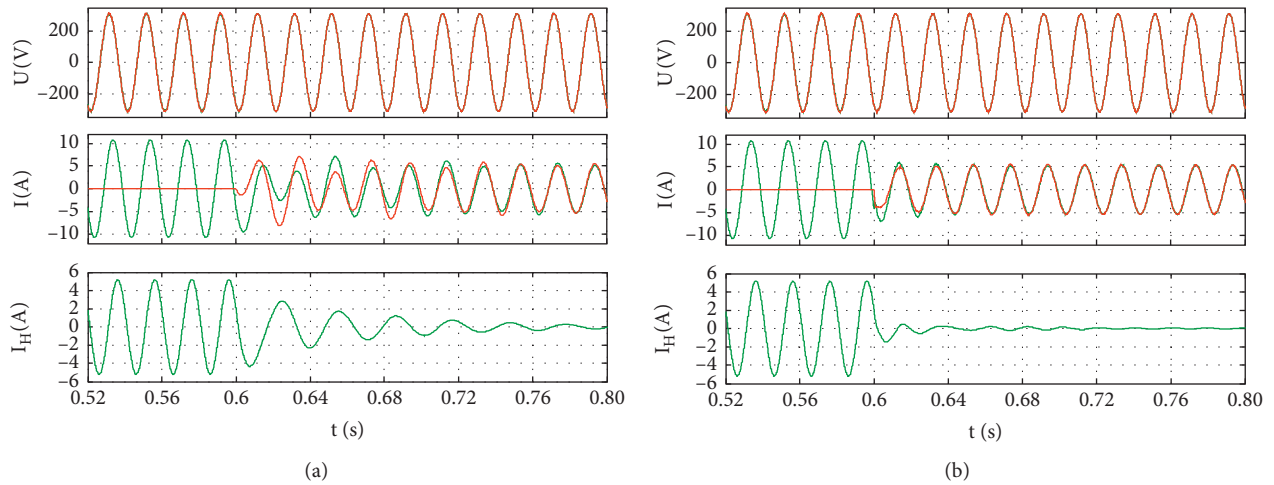
FIGURE 11: Output voltage, current, and circulating current of two parallel VSGs: (a) traditional virtual synchronization control strategy; (b) improved virtual synchronization control strategy.
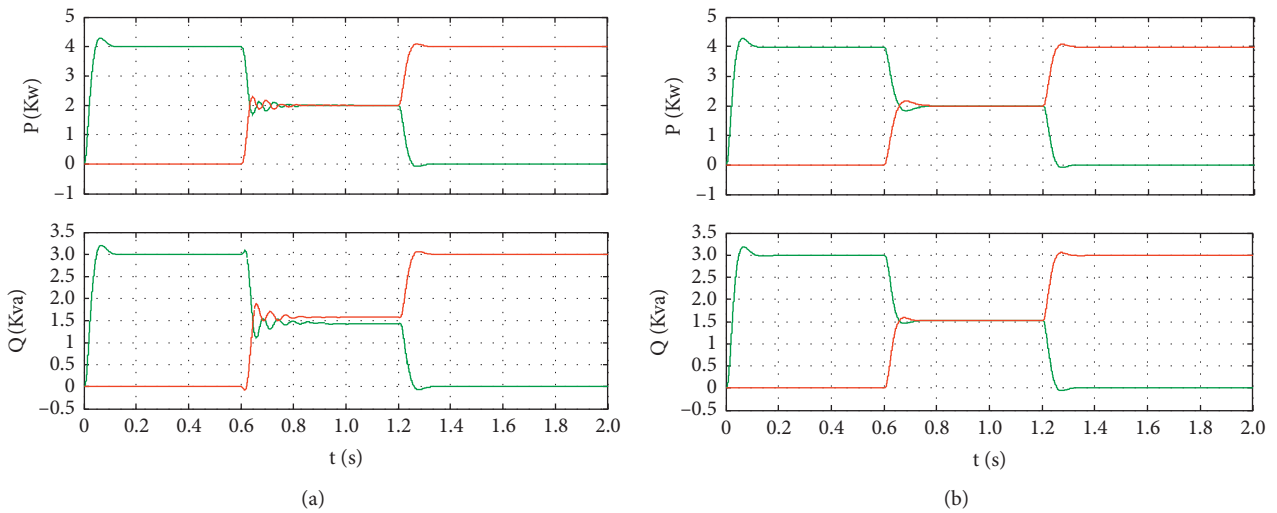

FIGURE 12: Output active power and reactive power of the parallel virtual synchronous control strategy: (a) traditional virtual synchronization control strategy; (b) improved virtual synchronization control strategy.
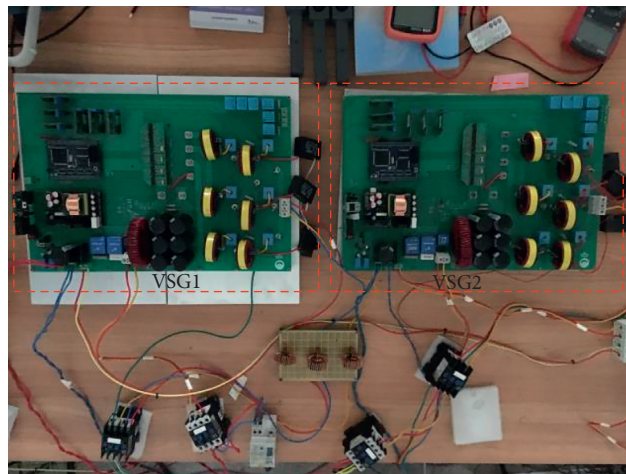

FIGURE 13: Pictures of the test platform.

TABLE 3: Experimental parameters.

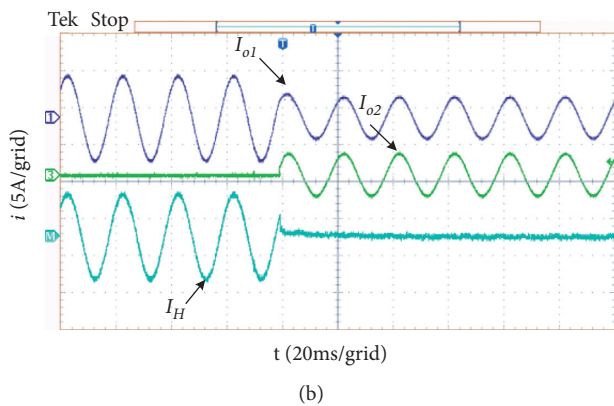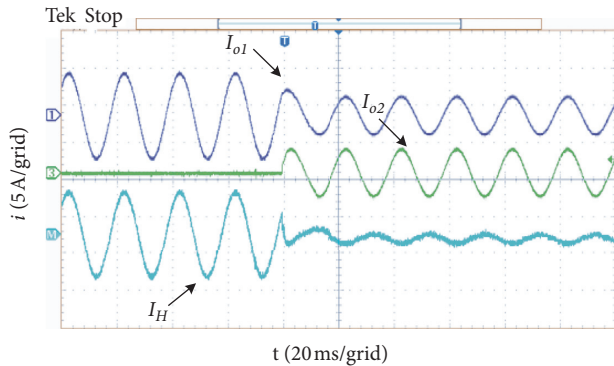| Parameter/unit	Value
U_{dc}/V	600
k_{up}	0.07
k_{ui}	5
D_{qi}	190
Z_{line1}/Ω	$0.4 + 0.06j$
Z_{line2}/Ω	$0.5 + 0.07j$
L_1/mh, R_1/Ω	5, 0.1
L_2/mh, R_2/Ω	4.8, 0.1
L_v/mh	1
U/V	380
J, D_p	0.02, 6
k_{ip}	2
K_e	0.2
Q_0/kvar	1
P_0/kW	3
P^*/kW	4
Q^*/kvar	1
R_v/Ω	-0.2

(a)

(b)

FIGURE 14: Output current and circulating current of two parallel VSGs: (a) traditional virtual synchronization control strategy; (b) improved virtual synchronization control strategy.

5. Conclusions

In this paper, the problems of power equipartitioning and circulating current suppression in the parallel operation mode of VSGs were studied. The conclusions and requirements for future work are as follows.

(1) When multiple VSGs are connected in parallel, the resistance and inductance characteristics of the transmission impedance cause the coupling between reactive power and active power. The reactive power distribution is affected by the droop coefficient, the reactive power reference value, and the transmission impedance. The current circulation of the parallel VSGs is affected by the deviation of output voltage and the value of transmission impedance.

(2) The virtual complex impedance including a resistive component and an inductive component is introduced into the inner voltage and current control loop. It reduces the coupling between active power and reactive power, and it reduces the disorderly distribution of power due to impedance differences. The load voltage control loop and integral part are introduced in the reactive power link of the VSG, which reduce the deviation of output voltage and restrain circulating current.

(3) According to the comparative analysis of the influence of control parameters and virtual complex impedance on the equivalent output impedance, the control parameters and virtual complex impedance are selected.

Data Availability

The data that support the findings of this study are included within the article.

Conflicts of Interest

The authors declare no conflicts of interest regarding the publication of this paper.

Acknowledgments

References

[1] T. W. Zheng, L. J. Chen, and S. W. Mei, "Review and prospect of virtual synchronous generator technologies," *Automation of Electric Power Systems*, vol. 39, no. 21, pp. 165–175, 2015.

[2] H. L. Hu, X. F. Wan, X. H. Ding et al., "An improved low voltage ride-through control strategy for distributed virtual synchronous generator," *Electric Machines and Control*, vol. 24, no. 1, pp. 145–155, 2020.

[3] Q.-C. Zhong and G. Weiss, "Synchronverters: inverters that mimic synchronous generators," *IEEE Transactions on Industrial Electronics*, vol. 58, no. 4, pp. 1259–1267, 2011.

[4] L. Y. Lu and C. C. Chu, "Consensus-based secondary frequency and voltage droop control of virtual synchronous generators for isolated AC micro-grids," *IEEE Journal on Emerging and Selected Topics in Circuits and Systems*, vol. 5, no. 3, pp. 443–455, 2015.

[5] K. Wang, L. Li, Y. Lan, and G. Xia, "Application research of chaotic carrier frequency modulation technology in two-stage matrix converter," *Mathematical Problems in Engineering*, vol. 2019, Article ID 2614327, 2019.

[6] Z. P. Lü, W. Z. Sheng, Q. C. Zhong et al., "Virtual synchronous generator and its applications in micro-grid," *Proceedings of the Chinese Society of Electrical and Electronics Engineers*, vol. 34, no. 6, pp. 2591–2603, 2014.

[7] Z. P. Lü, J. Su, R. Li, and H. Liu, "New power control strategy on paralleled micro-source inverters with different power levels," *Transactions of China Electrotechnical Society*, vol. 28, no. 7, pp. 191–198, 2013.

[8] Y. Du, J. H. Su, L. C. Zhang et al., "A mode adaptive frequency controller for microgrid," *Proceedings of the Chinese Society of Electrical and Electronics Engineers*, vol. 33, no. 19, pp. 67–75, 2013.

[9] J. Yao, H. B. Du, T. Zhou et al., "Improved droop control strategy for inverter parallel operation in micro-grid," *Power System Technology*, vol. 39, no. 4, pp. 932–938, 2015.

[10] M. R. Zhang, Z. C. Du, and S. B. Wan, "Research on droop control strategy and parameters selection for microgrids," *Transactions of China Electrotechnical Society*, vol. 29, no. 2, pp. 136–144, 2014.

[11] H. Zhang, F. Wan, X. Q. Li, and F. Yang, "Impedance matching strategy for parallel virtual synchronous generators," *Automation Electric Power System*, vol. 42, no. 9, pp. 69–74, 2018.

[12] L. J. Chen, Y. Y. Wang, T. W. Zhang, and T. Y. Chen, "Consensus-based distributed control of parallel-connected virtual synchronous generator," *Control Theory & Application*, vol. 34, no. 2, pp. 1084–1091, 2017.

[13] Q. H. Zhang, A. Luo, Y. D. Chen, and C. Peng, "Analysis of output impedance for parallel inverters and voltage control strategy," *Transactions of China Electrotechnical Society*, vol. 29, no. 6, pp. 98–105, 2014.

[14] Y. D. Chen and A. Y. Luo, "Circulating current analysis and robust droop multiple loop control method for parallel inverters using resistive output impedance," *Proceedings of the Chinese Society of Electrical and Electronics Engineers*, vol. 33, no. 18, pp. 18–29, 2013.

[15] Z. P. Lü and A. Luo, "Robust power control of paralleled micro-source inverters with different power ratings," *Proceedings of the Chinese Society of Electrical and Electronics Engineers*, vol. 32, no. 12, pp. 35–42, 2012.

[16] Q. C. Zhong, "Robust droop controller for accurate proportional load sharing among inverters operated in parallel," *IEEE Transactions on Industrial Electronics*, vol. 60, no. 4, pp. 1281–1290, 2012.

[17] S. Fan, T. J. Pu, G. Y. Liu et al., "Access technology of distributed power generation system in active power distribution network and its progress," *Transactions of China Electrotechnical Society*, vol. 31, no. 2, pp. 92–101, 2016.

[18] S. Fan, T. Pu, G. Liu, and Q. Chang, "Technologies and its trends of grid integration of distributed generation in active distribution network," *Transactions of China Electrotechnical Society*, vol. 31, no. 2, pp. 92–101, 2016.